Competing pairing interactions responsible for the large upper critical field in a stoichiometric iron-based superconductor $CaKFe_4As_4$

Matthew Bristow,[1,*] William Knafo,[2] Pascal Reiss,[1] William Meier,[3,4] Paul C. Canfield,[3,4] Stephen J. Blundell,[1] and Amalia I. Coldea[1,†]

[1]*Clarendon Laboratory, Department of Physics, University of Oxford, Parks Road, Oxford OX1 3PU, United Kingdom*
[2]*Laboratoire National des Champs Magnétiques Intenses (LNCMI), CNRS-UJF-UPS-INSA, Toulouse, France*
[3]*Ames Laboratory, Iowa State University, Ames, Iowa 50011, USA*
[4]*Department of Physics and Astronomy, Iowa State University, Ames, Iowa 50011, USA*

(Received 14 November 2019; accepted 2 March 2020; published 7 April 2020)

The upper critical field of multiband superconductors is an important quantity that can reveal details about the nature of the superconducting pairing. Here we experimentally map out the complete upper-critical-field phase diagram of a stoichiometric superconductor, $CaKFe_4As_4$, up to 90 T for different orientations of the magnetic field and at temperatures down to 4.2 K. The upper critical fields are extremely large, reaching values close to $\sim 3\,T_c$ at the lowest temperature, and the anisotropy decreases dramatically with temperature, leading to essentially isotropic superconductivity at 4.2 K. We find that the temperature dependence of the upper critical field can be well described by a two-band model in the clean limit with band-coupling parameters favoring intraband over interband interactions. The large Pauli paramagnetic effects together with the presence of the shallow bands is consistent with the stabilization of an FFLO state at low temperatures in this clean superconductor.

DOI: 10.1103/PhysRevB.101.134502

I. INTRODUCTION

The upper critical field, H_{c2}, is an important property of superconductors that defines their limit for practical applications. It also describes the complex interplay between different pairing gaps and symmetry and can shed light on the nature of the superconducting mechanism. Furthermore, the temperature dependence of the upper critical field can also provide evidence for the presence of the Fulde-Ferrell-Larkin-Ovchinnikov (FFLO) state [1,2], in which the order parameter varies in space. Iron-based superconductors have unusually large values of the upper critical field which reveal exotic effects caused by the interplay of orbital and paramagnetic pair-breaking in multiband superconductors with unconventional pairing symmetry [3]. They also provide the right conditions for the FFLO state to develop in clean materials due to the likely presence of shallow bands [4] and very large Pauli paramagnetic effects [1].

$CaKFe_4As_4$ is a clean and stoichiometric superconductor with a relatively high $T_c = 35$ K and it belongs to a family of 1144 iron-based superconductors [5]. This system lacks long-ranged magnetic order or a nematic electronic state at low temperatures [5–11] but, upon doping with Ni, a hedgehog magnetic structure is stabilized [9,12,13]. $CaKFe_4As_4$ has an exceptionally large critical current density due to strong pointlike defects caused by local structural site effects as well as surface pinning [14–16]. Due to reduced symmetry compared with the 122 family of iron-based superconductors, $CaKFe_4As_4$ is predicted to have up to ten different bands [Figs. 1(e) and 4]. However, angle-resolved photoemission spectroscopy (ARPES) detects a Fermi surface composed of three hole pockets and two electron pockets. The superconducting gaps are nearly isotropic and different for each of the Fermi surface sheets [4]. The presence of electron and hole sheets supports a spin resonance corresponding to the (π, π) nesting wave vector detected by neutron diffraction [6] and promotes a $s_{\pm}$ superconducting pairing symmetry in $CaKFe_4As_4$. Thus, this clean system is a model system for understanding the effect of pairing on its upper critical field.

To understand the superconducting properties of $CaKFe_4As_4$ we have measured the upper critical fields for two orientations in magnetic fields up to 90 T using electrical transport measurements. These experimental studies provide a complete $H_{c2}(T)$ phase diagram and allow us to model the entire temperature dependence, as previous work in magnetic fields up to 60 T could not reach the low-temperature region [7]. We find that $CaKFe_4As_4$ is highly isotropic at the lowest temperature. A two-band model describes the dependence of the upper critical fields for both directions and the band-coupling parameters indicate the presence of different pairing channels. At low temperatures, the upper critical field does not saturate but shows an upturn, consistent with the emergence of a FFLO state in $CaKFe_4As_4$.

II. EXPERIMENTAL DETAILS

Single crystals of $CaKFe_4As_4$ were grown in the Ames Laboratory, as discussed elsewhere [5,17]. Robust electrical

*Corresponding author: matthew.bristow@physics.ox.ac.uk
†Corresponding author: amalia.coldea@physics.ox.ac.uk

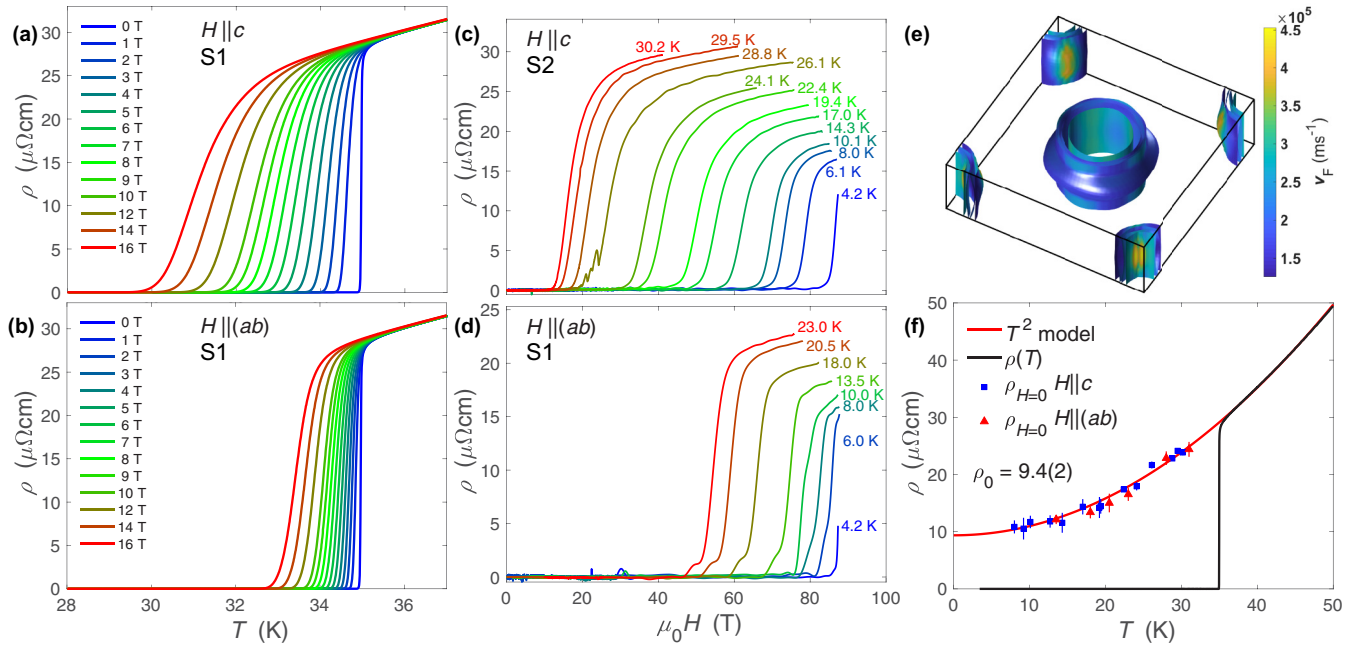

FIG. 1. Resistivity versus temperature for $CaKFe_4As_4$ (S1) at different constant magnetic fields for (a) $H||c$ and (b) $H||(ab)$. Resistivity versus magnetic field at constant temperatures measured concomitantly in pulsed fields up to 90 T, for (c) $H||c$ (S2) and (b) $H||(ab)$ (S1). (e) Fermi surface of $CaKFe_4As_4$ using experimental lattice parameters (as detailed in Fig. 4). The colors reflect the variation of the Fermi velocity. (f) Resistivity against temperature for sample S1 together with the zero-field extrapolated values from high fields shown in (c) and (d) [see also Fig. 5(d) in the Appendix]. The zero-temperature resistivity ρ_0 is estimated as $9.4(2)\,\mu\Omega$cm using a Fermi-liquid T^2 behavior [red line in (f)].

contacts were achieved using indium solder, giving contact resistances of less than 0.5 Ω. Samples were measured using the standard four- and five-point AC lock-in techniques and a current of 1 mA. We investigated several high-quality single crystals, with large residual resistivity ratios ∼14.5 [RRR = $\rho(300\,\text{K})/\rho(36\,\text{K})$], small residual resistivity, $\rho_0 \sim 9.4\,\mu\Omega$cm, and sharp superconducting transitions, $\Delta T_c \sim 0.1$ K [see Figs. 1(f) and 5(c)]. Transport measurements were performed in Oxford up to 16 T in a Quantum Design PPMS in constant magnetic fields and for different magnetic field orientations [$H||c$ and $H||(ab)$]. Pulsed magnetic-field measurements were performed at LNCMI Toulouse, using a 70 T single coil and a 90 T dual coil at constant temperatures below 35 K for both field orientations (an example is shown in Fig. 6).

III. UPPER CRITICAL FIELD FROM TRANSPORT MEASUREMENTS

Figure 1(a)–1(b) shows resistivity against temperature for different fixed magnetic fields for orientations of the sample in relation to the applied magnetic field. As the magnetic field increases, the superconducting transition becomes broader and suppressed faster for $H||c$ by 5 K in 16 T [Fig. 1(a)], as compared with the $H||(ab)$ case for which H_{c2} only changes by 2 K in 16 T [Fig. 1(b)], as the orbital effects are less effective in suppressing superconductivity in this orientation. These data are used to extract the upper critical field near T_c, defined as the offset field, as shown in Figs. 5(a) and 5(b). Due to the high crystallinity of our samples that display sharp superconducting transitions, we find that the critical temperature from magnetization measurements is similar to the offset temperature determined from transport measurements [Fig. 5(a)]. To completely suppress the superconductivity of $CaKFe_4As_4$, we have used pulsed magnetic fields up to 90 T. Resistivity data against magnetic fields up to 90 T measured at fixed temperature are shown in Figs. 1(c) and 1(d) for the two different orientations. Despite the strong disparity in the degree of suppression of superconductivity between the two field directions close to T_c, at the lowest measurable temperature of 4.2 K, the normal state is reached at a similar field ∼85 T for both orientations.

IV. UPPER-CRITICAL-FIELD PHASE DIAGRAM

Based on these experimental data, we have constructed the complete upper-critical-field phase diagram of $CaKFe_4As_4$ down to 4.2 K as shown in Fig. 2(a) for the two orientations. Our results are in good agreement with previous studies up to 60 T for both offset and onset critical fields [7] [see Figs. 9(a) and 9(b)] and reveal extremely large upper critical fields, reaching almost $\sim 3\,T_c$ at the lowest temperatures. These values are above the Pauli paramagnetic limit, $\sim 1.85\,T_c$, estimated to be ∼65 T for a single-band superconductor and assuming $g = 2$ and the weak-coupling limit. The anisotropy of the upper critical field, defined as the ratio of the upper critical field for different orientations, $\Gamma = H_{c2}^{ab}/H_{c2}^{c}$, drops dramatically with decreasing temperature from ∼4 to 1, as shown in Fig. 2(b). Interestingly, the upper critical fields for the two orientations cross at $T \sim 4.2$ K, leading to isotropic superconducting behavior in the low-temperature limit. This phenomenon has been found in optimally doped

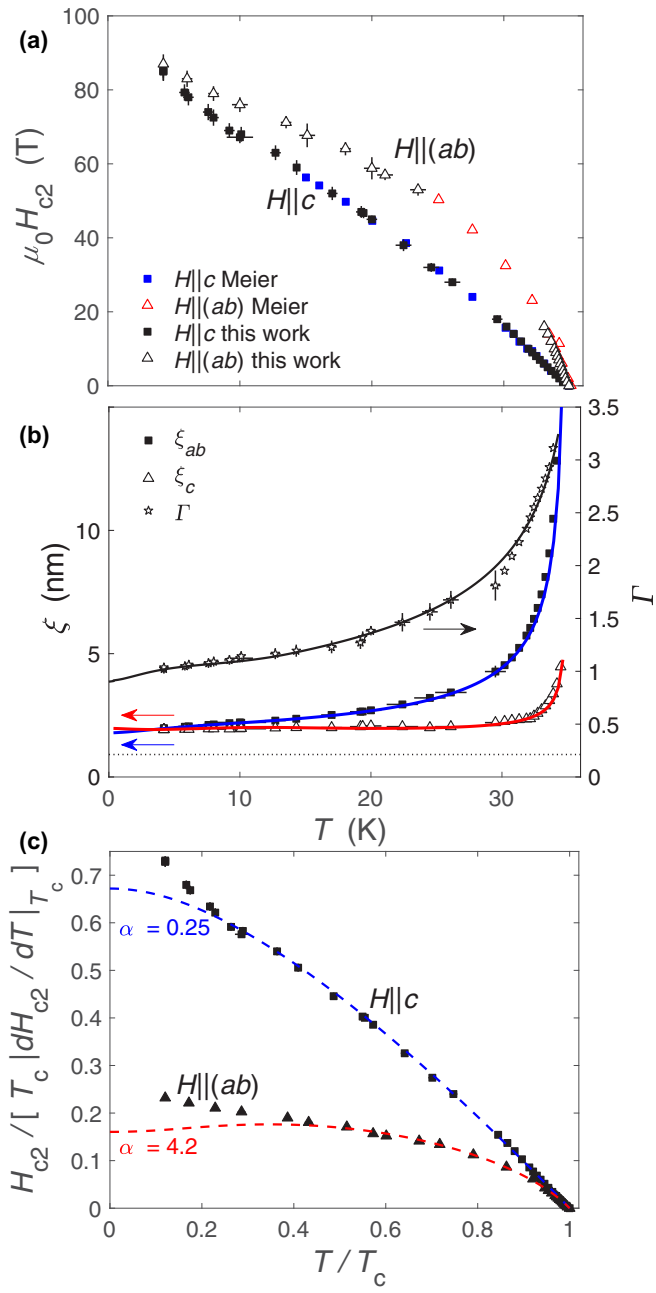

FIG. 2. (a) Upper critical fields as a function of temperature in $CaKFe_4As_4$ when $H||c$ (solid squares) and $H||(ab)$ (open triangles), together with previous reported data measured up to 60 T from Ref. [7]. (b) The temperature dependence of coherence length extracted close to T_c, as described in the Supplemental Material. The $H_{c2}(T = 0)$ values were used to find the zero-temperature coherence lengths. The horizontal dashed line represents the 3D-2D crossover when coherence length $\sim c/\sqrt{2}$. The anisotropy $\Gamma = H_{c2}^{ab}/H_{c2}^{c}$ on the right axis approaches $\Gamma = 1$ at ~4.2 K. Solid lines are guides to the eye. (c) Upper critical fields for $H||c$ (black squares) and $H||(ab)$ (black triangles) scaled by the superconducting transition temperature, T_c, and the slope near T_c from the WHH model against reduced temperature T/T_c. The dashed blue and red lines are fits to the WHH model for $H||c$ and $H||(ab)$ using different values of α. Deviation from the WHH model occurs at low temperatures for both field orientations.

iron-based superconductors, such as $FeSe_{0.5}Te_{0.5}$ [18,19] and $(Ba,K)Fe_2As_2$ [20]. This behavior reflects the large Pauli paramagnetic effects in iron-based superconductors and the influence of Fermi surface details on limiting the orbital effects [20]. The Fermi surface of $CaKFe_4As_4$ has significant warping for the outer electron and hole band that can potentially allow circulating currents out of plane [see Fig. 4(d) in the Appendix]. Furthermore, the calculated anisotropy of the penetration depth based on plasma frequencies (as in Ref. [21]) is $\Gamma = \lambda_c/\lambda_{ab} \sim 4.5$, (see Fig. 4) similar to the measured anisotropy close to T_c [Fig. 2(b)], suggesting that the Fermi surface details play an important role in understanding its superconducting properties.

Having experimentally determined the upper critical fields for different orientations in magnetic field, we can extract the associated coherence lengths in different temperature regimes, as detailed in the Appendix. In the vicinity of T_c, the Ginzburg-Landau coherence lengths shown in Fig. 2(b) are $\xi_{ab}^{GL} = 1.66(4)$ nm and $\xi_c^{GL} = 0.53(2)$ nm for $CaKFe_4As_4$, similar to previously reported values [7]. In the low-temperature limit, we find coherence lengths of $\xi_{ab} = 1.83(3)$ nm and $\xi_c = 1.87(6)$ nm, as shown in Fig. 7. This demonstrates the presence of an isotropic superconducting state at lowest temperature in $CaKFe_4As_4$. The coherence lengths approach the 3D to 2D crossover close to $c/\sqrt{2} \sim 0.911$ nm, as shown in Fig. 2(b) [5,22]. The low-temperature extracted ξ values are larger than ~0.7 nm reported from scanning tunnelling microscopy (STM) measurements, which probe locally the vortex lattice rather than an overall averaged effect [23]. Knowing the coherence length allows us to estimate the depairing current density, J_d, as described in the Appendix [24]. Previous magnetization data reported a value of $\mu_0 H_{c1} = 22(1)$ mT when $H||c$ at low temperatures which, combined with H_{c2} reported here, give $\kappa \sim 99(2)$ and $\lambda = 183(6)$ nm. Using this value for the penetration depth and $\xi = 1.86(3)$ nm gives $J_d = 1.61(9) \times 10^8$ A/cm^2, which is one of the largest among iron-based superconductors. This supports the extremely large critical current densities, reported previously for $CaKFe_4As_4$ in Ref. [14]. The small coherence length of $CaKFe_4As_4$ is compatible with the presence of the large upper critical field, consistent with small Fermi velocities and high T_c values of $CaKFe_4As_4$ ($\xi \sim \hbar v_F/(2\pi k_B T_c)$ [1]). Surface superconductivity can survive in a thin layer of thickness $\sim\xi$ in systems with clean surfaces and it can lead to a critical field larger than H_{c2}. To establish the importance of those effects, future angular-dependent studies would be necessary to identify the role played by surface superconductivity in $CaKFe_4As_4$ close to T_c. Using the extrapolated zero-temperature normal state resistivity $\rho_0 \sim 9.4\,\mu\Omega$cm in Fig. 1(f) and carrier concentrations from Ref. [7], we can estimate a mean-free path of $\ell = 26.6$ nm. Since the mean-free path due to elastic scattering from impurities is far larger than the coherence length, $\xi(0) \ll \ell$, $CaKFe_4As_4$ can be described as being in the clean limit. Resistivity data in Fig. 1(f) also show a sharp superconducting transition indicating a high-quality single crystal. Furthermore, the extrapolated high-field resistivity at low temperatures [see Fig. 4(d)] displays a T^2 dependence indicative of a Fermi-liquid behavior that extends up to ~55 K.

To assess the role of orbital and Pauli paramagnetic effects on the upper critical field of $CaKFe_4As_4$, we first describe the temperature dependence of the upper critical field using the three-dimensional Werthamer-Helfand-Hohenberg (WHH) model [25], with the inclusion of spin paramagnetism effects. The slope close to T_c ($H'_{c2} = -|dH_{c2}/dT|_{T=T_c}$) is used to estimate the zero-temperature orbital upper critical field and $H_{c2}^{orb} = 0.73T_cH'_{c2}$ for the clean limit ($0.69T_cH'_{c2}$ in the dirty limit) for a single-band weak-coupling superconductor with ellipsoidal Fermi surface [26]. We find that the orbital pair breaking dominates the temperature dependence for $H||c$ down to 10 K, below which it deviates, as shown in Fig. 2(c). However, when the magnetic field is aligned along the conducting (ab) plane, a Pauli pair-breaking contribution has to be included which reduces the orbital-limited critical field by $\mu_0 H_P = \mu_0 H_{c2}^{orb}/\sqrt{1+\alpha^2}$, where α is the Maki parameter. The extracted Maki parameter α is small where the orbital effects dominate ($\alpha \sim 0.25$ for $H||c$), but it becomes significant reaching $\alpha = 4.2$ for $H||(ab)$ [see Fig. 2(c)]. This value is close to that of $FeSe_{0.6}Te_{0.6}$ single crystals where $\alpha \sim 5.5$, suggesting that the upper critical field is dominated by Pauli paramagnetic effects [27]. Strong paramagnetic effects are an important signature of optimally doped iron-based superconductors [28–32]. For a clean isotropic single band, the Maki parameter is given by $\alpha = \pi^2\Delta/(4E_F)$. The values of the measured superconducting gap Δ varies between $2.4 - 13$ meV whereas the Fermi energies vary significantly for different bands, being smallest for the inner hole band, α ($\sim$3 meV) and the shallow electron band δ ($\sim$10 meV) [4,33]. The band-structure calculation predicts four electron pockets centered at the M point, as shown in Fig. 4. Experimentally, only one electron pocket can be resolved in experiments due to a significant intrinsic linewidth and the fact that the bottom of these bands is located very close to Fermi level [4]. Thus, the presence of the shallow bands, together with the small Fermi energies E_F and large superconducting gap Δ create conditions for large α and Pauli pair-breaking.

V. UPPER CRITICAL FIELD DESCRIBED BY A TWO-BAND MODEL

To describe the complete temperature dependence of $H_{c2}(T)$ for $CaKFe_4As_4$, including the upturn below $\sim$10 K for both orientations, a two-band model in the clean limit is considered, as detailed in Ref. [1] and in the Appendix. This model accounts for the presence of two different bands with interband scattering (λ_{11}, λ_{22}) and intraband effects (λ_{12}, λ_{21}) and includes paramagnetic effects and allows for the presence of an FFLO inhomogeneous state at high fields and low temperatures [1]. An FFLO state is characterized by a real-space modulation of the superconducting order parameter either in amplitude or phase such that the system energy is minimized under the constraints of a large Zeeman energy and superconducting condensation energy [2]. As the FFLO wave vector Q appears spontaneously below a certain temperature, T_{FFLO}, the spinodal instability line in $H_{c2}(T)$ at a finite Q acquires the characteristic upturn [1].

In most iron-based superconductors, the pairing is expected to be mediated by spin fluctuations leading to a sign changing $s_\pm$ order parameter. In this case, upper critical fields are generally described by dominant interband coupling parameters with $\lambda_{11} = \lambda_{22} = 0$ and $\lambda_{12} = \lambda_{21} \sim 0.5$ ($\lambda_{11}\lambda_{22} \ll \lambda_{12}\lambda_{21}$) [3,7,28,29,34,35]. Furthermore, in these multiband systems, orbital fluctuations can dominate the pairing interactions in certain conditions favoring a gap with equal sign on each pocket, resulting in the s^{++} pairing [36] ($\lambda_{11}\lambda_{22} \gg \lambda_{12}\lambda_{21}$).

To model the upper critical fields for both field orientations, we have considered different input parameters from previous experiments on $CaKFe_4As_4$. For example, the ratio between the extreme velocities of the Fermi surfaces is taken from ARPES experiments [33] and gives a starting value of $\eta_c \sim 0.02$, which is the squared velocity ratio between the two bands. Upper critical field simulations have a strong sensitivity to η values, as shown in Fig. 8 in the Appendix, and it can change for different field orientations due to differences in the in-plane velocities on the Fermi surface [see Figs. 1(e) and 4]. We assume that $s = 1$ [defined by Eqs. (A9) in the Appendix)] for both field orientations and the starting values of the Maki parameters are those from the single band model of $H_{c2}(T)$ in Fig. 2(c).

First, the $H_{c2}(T)$ data are simulated for $CaKFe_4As_4$ using parameters corresponding to the $s^\pm$ case [dashed lines Figs. 3(a) and 3(b)], which provide a reasonable representation of the observed behavior for both orientations. However, we find that $H_{c2}(T)$ is best described using $\lambda_{11} = 0.81$, $\lambda_{22} = 0.29$, and $\lambda_{12} = \lambda_{21} = 0.1$ [solid lines in Figs. 3(a) and 3(b)], which is consistent with s^{++} pairing. For the later model, the constrained Fermi velocities are $v_1 \sim 380(20)$ meVÅ and $v_2 \sim 54(4)$ meVÅ when $H||c$, and $v_1 \sim 195(20)$ meVÅ and $v_2 \sim 41(4)$ meVÅ when $H||(ab)$ (see Table I). The values of v_2 are similar in both orientations, indicative of a strongly warped sheet (see Fig. 4). On the other hand, v_1 is larger for $H||c$ and is close to $\sim$360 meVÅ, reported for the α hole band from ARPES measurements [33]. The band-coupling constants, $\lambda_{i,j}$, that describe our data, suggest that the interband scattering due to spin fluctuations is dominated by the intraband effects in $CaKFe_4As_4$, which can occur in the presence of strong orbital fluctuations [36]. For s^{++} pairing to overcome $s^\pm$ pairing normally requires the presence of strong disorder, which leads to similar superconducting gaps on different Fermi surfaces [37]. Furthermore, the band coupling constants for the s^{++} case resemble those used to describe a two-band superconductor in the dirty limit [38]. However, $CaKFe_4As_4$ is clean, suggesting that disorder effects are negligible. Thus, based on the band-coupling parameters, we conclude that orbital fluctuations may dominate over spin fluctuations.

When the magnetic field lies along the conducting planes, the low-temperature upturn of $H_{c2}(T)$ in Fig. 3(b) cannot be fully captured by only considering the two-band model with large Pauli paramagnetic effects, $\alpha \sim 3.2$. The formation of the FFLO state in a system with a cylindrical Fermi surface requires a large Zeeman energy and a critical Maki's parameter of $\alpha_c = 4.76$ [2], compared to $\alpha_c = 1.8$ [39] for a three-dimensional Fermi surface. $CaKFe_4As_4$ has a complex Fermi surface with two-dimensional cylindrical and highly warped sheets and together with a large value of α creates the conditions for the emergence of an FFLO state [1]. A FFLO state

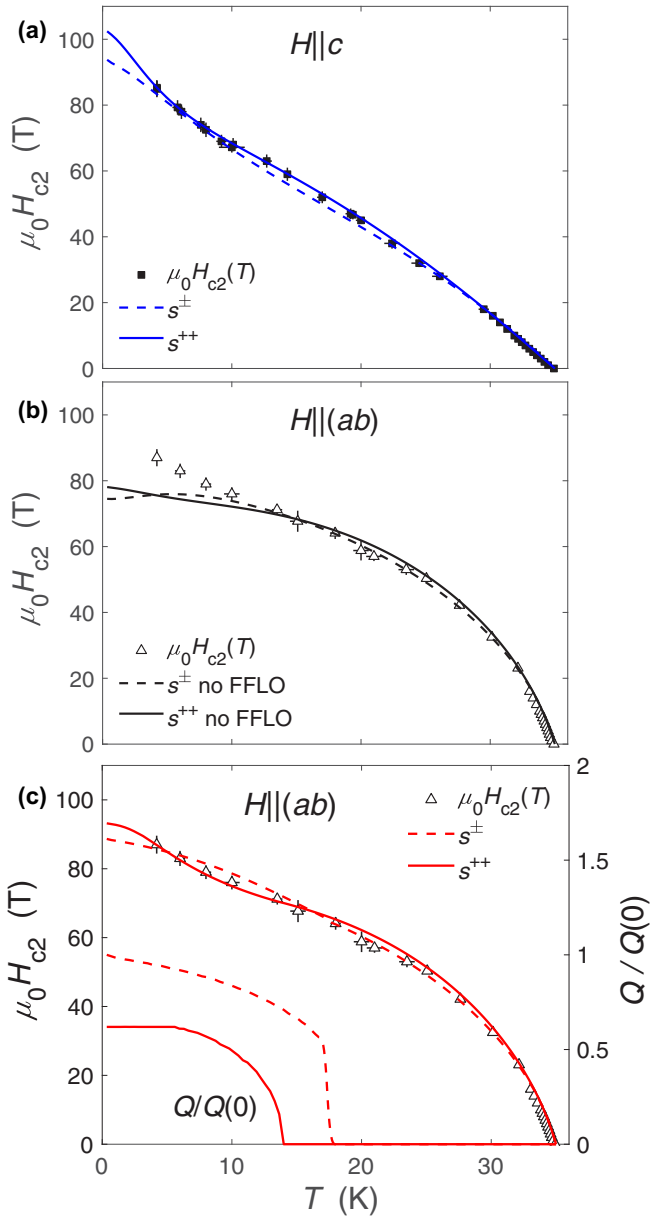

FIG. 3. Upper critical fields for (a) $H||c$ (solid squares) and (b), (c) $H||(ab)$ (open triangles) described by the two-band model. The dotted lines correspond to $s^{\pm}$ pairing [$\lambda_{11} = \lambda_{22} = 0$, $\lambda_{12} = \lambda_{21} \sim 0.5$, $\alpha_1 = 0.95$, $\alpha_2 = 0$ for $H||c$ and $\alpha_1 = 3.1$ and $\alpha_2 = 0.7$ for $H||(ab)$]. Solid lines represent s^{++} pairing [$\lambda_{11} = 0.81$, $\lambda_{22} = 0.29$ and $\lambda_{12} = \lambda_{21} = 0.1$, $\alpha_1 = 0.5$ for $H||c$ and $\alpha_1 = 3.2$, $\alpha_2 = 0$ for $H||(ab)$]. The values of η vary between ~0.02 in (a) and ~0.04 in (b). (c) The temperature dependence of the upper critical field including the emergence of the FFLO state for the two different pairing symmetries with the same parameters as in (b). The lower dashed and red lines represent the scaled FFLO $Q/Q(0)$ modulation for $H||(ab)$ for the respective pairing (right axis).

can be realized in very clean materials with weak scattering of quasiparticles and it generally manifests as change in slope in the upper critical field at low temperatures [1]. We find indeed that to describe the upper critical field data of $CaKFe_4As_4$ over the entire temperature range, a FFLO state could be stabilized below $T_{FFLO} \sim 14$ K, as shown in Fig. 3(c). Possible contenders to support such an effect are the shallow electron Fermi surface pocket, δ, in the zone corner which is very close to the Fermi level (~10 meV) as well as the inner hole band α (~3 meV), as detected by ARPES measurements [4].

The temperature dependence of the upper critical field data in $CaKFe_4As_4$ implies that the intraband scattering is likely to dominate the interband scattering, the latter of which is promoted by spin fluctuations. In the presence of spin-orbit coupling, the orbital fluctuations can lead to s^{++} pairing, as suggested for LiFeAs [40]. Usually, s^{++} pairing results in far lower critical fields than $s^{\pm}$ pairing [1], so our results for $CaKFe_4As_4$ are somehow unusual as H_{c2} is almost $3\,T_c$ at the lowest temperature. The presence of several scattering channels in a multiband system like $CaKFe_4As_4$ can increase the upper critical field to a much greater extent than in single gap superconductors, caused by the relative weight of different scattering channels. $CaKFe_4As_4$ theoretically has up to six large cylindrical hole bands, (with the equivalent of 50% hole doping in a 122 iron-based superconductor) providing a large density of states (see Figs. 1(e) and 4 and Ref. [33]) and it can also promote intraband scattering driven by orbital or electron-phonon couplings. On the other hand, the shallow bands in $CaKFe_4As_4$ are likely to be involved in the stabilization of the FFLO state. Thus, the temperature dependence of the upper critical field of $CaKFe_4As_4$ can reflect the behavior of two dominant superconducting gaps that reside on different sheets of the cylindrical Fermi surface, possibly one on a large hole band and another on a shallow small band. A theoretical work studying the superconducting instabilities in $CaKFe_4As_4$ also found two different symmetry representations of the superconducting gap suggesting different pairing interactions, involving both conventional $s\pm$ wave but also pairing that would lead to additional sign change within the hole and electron pockets [41]

In summary, we have experimentally mapped the upper critical fields of $CaKFe_4As_4$ up to 90 T and down to 4.2 K, providing a complete phase diagram for this stoichiometric superconductor. The anisotropy decreases dramatically with temperature, the system becoming essentially isotropic near 4 K. Upper critical fields are extremely large in this system, reaching close to $\sim 3\,T_c$ at the lowest temperature, well above the expectation based on conventional single-band superconductivity. Instead, the temperature dependence of the upper critical field can be described using by a two-band model in the clean limit. The band-coupling constants suggest a dominant orbital pairing over spin fluctuations pairing in $CaKFe_4As_4$. Furthermore, for magnetic fields aligned in the conducting plane and due to large Pauli paramagnetic effects, we find that the temperature dependence of the upper critical field is consistent with the emergence of an FFLO state at low temperatures.

In accordance with the EPSRC policy framework on research data, access to the data will be made available [42].

ACKNOWLEDGMENTS

We thank Alex Gurevich for helpful discussions related to the two-band modeling of the upper critical field and Jérôme Béard, Marc Nardone, and Abdelaziz Zitouni

for the technical support during the pulsed field experiments. This work was mainly supported by Oxford Centre for Applied Superconductivity and EPSRC Grants (No. EP/I004475/1 and No. EP/EP/I017836/1). P.R. acknowledges the support of the Oxford Quantum Materials Platform (Grant No. EP/M020517/1). Part of this work was supported HFML-RU/FOM and LNCMI-CNRS, members of the European Magnetic Field Laboratory (EMFL) and by EPSRC (UK) via its membership to the EMFL (Grant No. EP/N01085X/1). Part of this work at the LNCMI was supported by Programme Investissements d'Avenir under Program No. ANR-11-IDEX-0002-02, Reference No. ANR-10-LABX-0037-NEXT. Work at Ames Laboratory was supported by the U.S. Department of Energy, Office of Basic Energy Science, Division of Materials Sciences and Engineering. Ames Laboratory is operated by the U.S. Department of Energy by Iowa State University under Contract No. DE-AC02-07CH11358. W.M. was supported by the Gordon and Betty Moore Foundation's EPiQS Initiative through Grant No. GBMF4411. We also acknowledge financial support of the John Fell Fund of the Oxford University. A.I.C. acknowledges an EPSRC Career Acceleration Fellowship (No. EP/I004475/1) and Oxford Centre for Applied Superconductivity [43].

APPENDIX

In this Appendix, we present additional data to support the findings presented in the main paper.

1. Experimental details.

Several high-quality single crystals were used in this study with large residual resistivity ratios RRR = $\rho(300\,\mathrm{K})/\rho(36\,\mathrm{K}) \sim 14.5$, small ρ_0 values of $\sim 9.2\,\mu\Omega$cm and sharp superconducting transitions with $\Delta T_c \sim 0.1\,\mathrm{K}$, as shown in Figs. 5(c) and 1(f). Temperature sweeps were performed at constant magnetic field for different orientations, $H||c$ and $H||(ab)$ to build the high-temperature part of the $H_{c2}(T)$ phase diagram. Magnetic fields up to 90 T were produced by using current pulses through two different solenoid coils. An example of the magnetic field produced as a function of time is shown in Fig. 6.

2. Determining superconducting coherence lengths

The superconducting coherence lengths can be found in both field orientations near T_c using the Ginzburg-Landau (GL) approach from the equations

$$\xi_{ab}^{GL} = \sqrt{\frac{\Phi_0}{2\pi\mu_0 \left|\frac{dH_{c2}^{c}}{dT}\right|_{T_c} T_c}}, \xi_c^{GL} = \frac{\Phi_0}{2\pi\mu_0 \left|\frac{dH_{c2}^{ab}}{dT}\right|_{T_c} T_c \xi_{ab}^{GL}}, \tag{A1}$$

where Φ_0 is the magnetic flux quanta, $\mu_0|dH_{c2}^{c}/dT|_{T_c}$ is the slope near T_c when $H||c$, $\mu_0|dH_{c2}^{ab}/dT|_{T_c}$ is the slope near T_c when $H||(ab)$, and ξ_{ab}^{GL} and ξ_c^{GL} are the respective GL coherence lengths.

At the lowest temperature, the coherence lengths are extracted using $\mu_0 H_{c2}(T \to 0)$ and the following equations:

$$\xi_{ab} = \sqrt{\frac{\Phi_0}{2\pi\mu_0 H_{c2}^{c}(T \to 0)}}, \quad \xi_c = \frac{\Phi_0}{2\pi\mu_0 H_{c2}^{ab}(T \to 0)\xi_{ab}}, \tag{A2}$$

where ξ_{ab} and ξ_c are the coherence lengths in the (ab) plane and along the c axis, and $\mu_0 H_{c2}^{c}(T \to 0)$ and $\mu_0 H_{c2}^{ab}(T \to 0)$ are the critical fields at the lowest temperature when $H||c$ and $H||(ab)$, respectively (see Fig. 7). Using Eqs. (A2) at different constant temperatures, one can estimate $\xi_i \to \xi_i(T)$ and $H_{c2} \to H_{c2}(T)$, and the anisotropy ratio, Γ, as shown in Fig. 2(b) in the main text and Fig. 7.

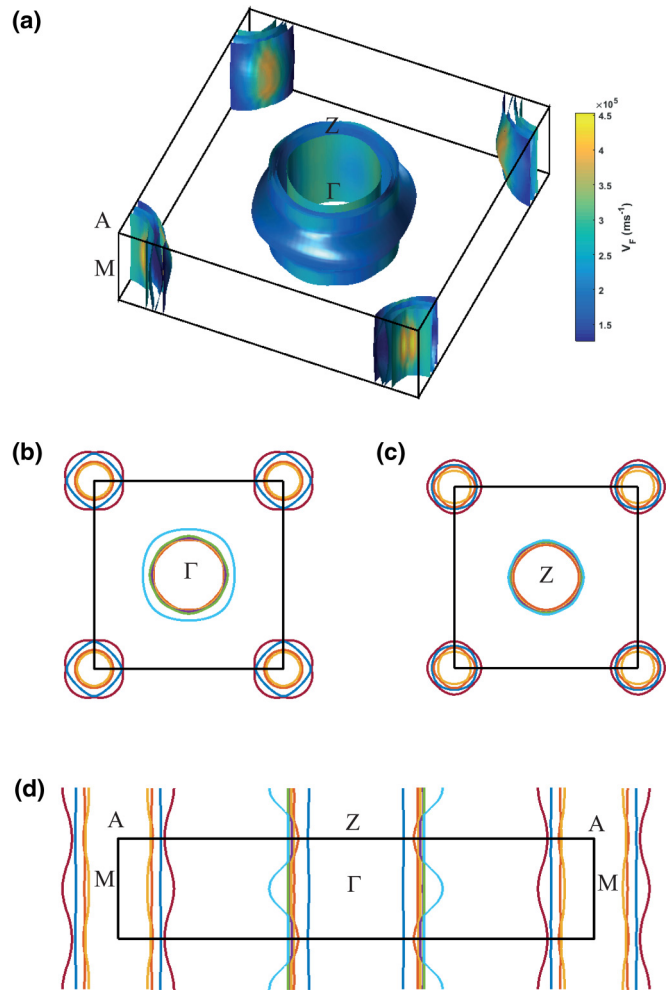

FIG. 4. Fermi surface of $CaKFe_4As_4$.(a) Fermi surface with velocity color. Slices at the (b) Γ and (c) Z point, indicating the size of the different sheets. Solid lines indicate the Brillouin zone. (d) Fermi surface slice along the [110] diagonal of the Brillouin zone indicated by the solid lines. The calculations were performed using WIEN2K and GGA approximation and the experimental lattice parameters described by the $P4/mmm$ symmetry group were $a = b = 3.86590$ Å, $c = 12.88400$ Å [5]. The calculated value of anisotropy, $\Gamma = \lambda_c/\lambda_{ab} = 313.68/70 = 4.5$, using a similar approached used in Ref. [21]. These calculations are in agreement with previous results reported in Ref. [22].

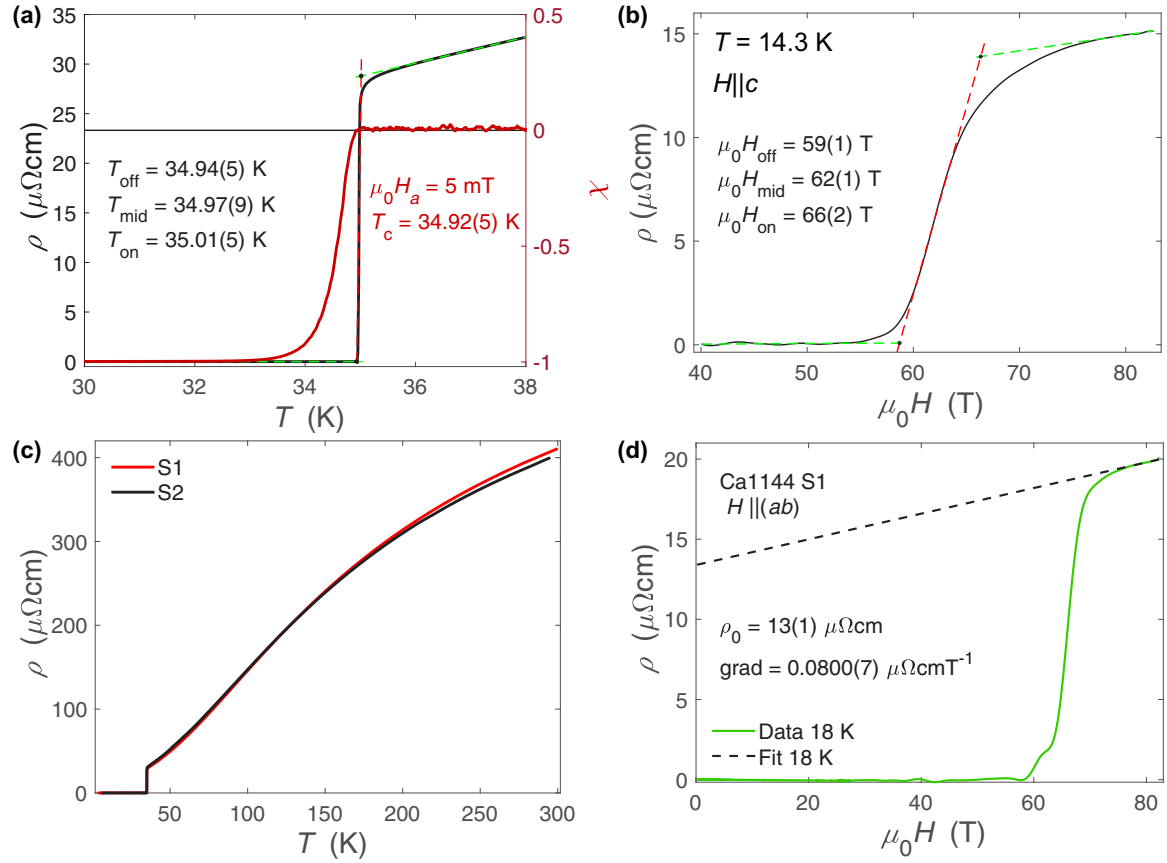

FIG. 5. Transport data of $CaKFe_4As_4$ as a function of temperature and magnetic field. (a) Estimating the critical temperature, T_c, from resistivity against temperature in zero magnetic field (left axis) and from magnetic susceptibility in a small applied field of 5 mT (right axis). The midpoint of the transition, T_{mid}, is identified as the peak in the derivative $d\rho/dT$. Linear fits are performed above and below the midpoint transition and the intercepts are defined as T_{off} and T_{on}, as labeled in the figure. T_c from susceptibility is defined as the point at which diamagnetism occurs and deviates from the high-temperature background and it is closest to the offset temperature in transport. The critical temperatures used to build the phase diagrams in magnetic field were extracted using T_{off} from the transport data. (b) The estimation of the upper critical field, H_{off}, from resistivity in pulsed magnetic field data measured at constant temperature using the same method as in (a). (c) Resistivity against temperature for different samples of $CaKFe_4As_4$ between 300 K and 2 K. The superconducting transition is very sharp, with $T_{c,0} = 35.0$ K and width $\Delta T_c = 0.15$ K, values typical for all measured single crystals indicating their high quality. (d) Resistivity data as a function of magnetic field for the sample S1 when $H||(ab)$ at 18 K. The dashed black line shows the linear extrapolation used to obtain the zero-field resistivity at 18 K and the intercept, $\rho_{H\to 0}(T)$, and gradient are shown. Using this method, the extracted values of zero-field resistivity measured at constant temperatures are shown in Fig. 1(f).

3. Depairing current density

Using the coherence length, one can also determine the critical depairing current density of a superconductor, J_d. As a function of temperature and magnetic field, this is expressed as [24]

$$J_d(T,H) = \frac{2}{3\mu_0\lambda^2(T)}\sqrt{\frac{\mu_0\left(H_{c2}^2(T)-H^2\right)^{1/2}\Phi_0}{6\pi}}, \quad \text{(A3)}$$

where λ is the superconducting penetration depth and Φ_0 is the magnetic flux quantum. At zero temperature and in no magnetic field, this gives

$$J_d(0,0) = \frac{2}{3\mu_0\lambda^2(0)}\sqrt{\frac{\mu_0 H_{c2}(0)\Phi_0}{6\pi}}. \quad \text{(A4)}$$

Substituting $\mu_0 H_{c2} = \Phi_0/2\pi\xi^2$, this equation can be rearranged to give

$$J_d(0,0) = \frac{\Phi_0}{3\sqrt{3}\pi\mu_0}\frac{1}{\lambda^2(0)\xi(0)}. \quad \text{(A5)}$$

Previous magnetization reported $\mu_0 H_{c1} = 22(1)$ mT [14] when $H||c$ at low temperature which, combined with H_{c2} values reported here, give $\kappa \sim 99(2)$ and $\lambda = 183(6)$ nm. Using $\xi = 1.86$ nm, we find that the depairing current density is $J_d \sim 1.62 \times 10^8$ A/cm^2, which is among the largest of any known iron-based superconductor.

4. The upper critical fields using a two-band model

To describe the entire temperature dependence of $H_{c2}(T)$ for $CaKFe_4As_4$, including the upturn below ~10 K for both orientations, we use a two-band model in the clean limit.

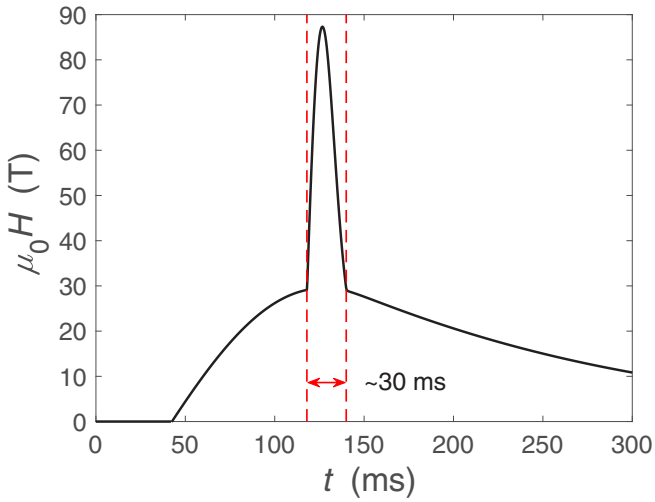

FIG. 6. Generation of the high-magnetic field pulse. Applied magnetic field as a function of time from the 90 T magnet in Toulouse. The peak of this pulse was ~88 T and is generated by overlaying pulsed current though two different coils. The pulse on the inner coil which generates the extremely high fields lasts ~30 ms.

This models includes paramagnetic effects and allows the emergence of a FFLO state, as detailed in Ref. [1]. The values of the upper critical field for different temperatures are found from estimating the following expressions:

$$a_1[\ln t + U_1] + a_2[\ln t + U_2] + [\ln t + U_1][\ln t + U_2] = 0, \tag{A6}$$

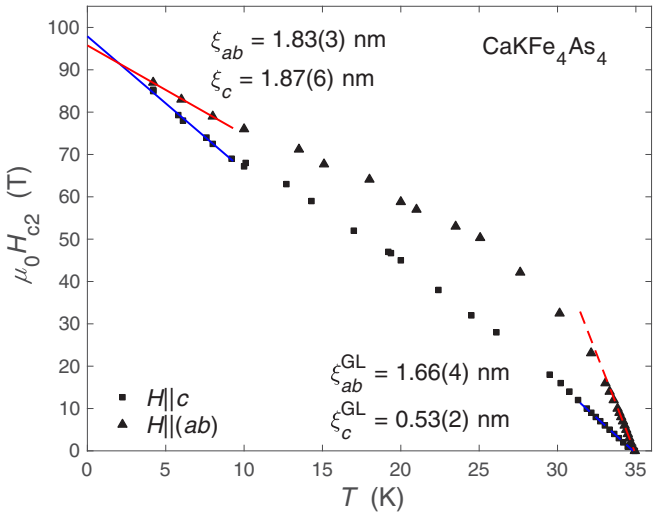

FIG. 7. Coherence length extraction. Upper critical fields in $CaKFe_4As_4$ as a function of temperature. The dashed blue and red lines are linear fits near T_c when $H||c$ and $H||(ab)$, respectively. The gradients of these fits (shown in the figure) were used to calculate the coherence lengths using the Ginzburg-Landau theory [Eq. (A1)]. The solid blue and red lines are linear fits to the low-temperature region when $H||c$ and $H||(ab)$, respectively. The zero-temperature extrapolation of $H_{c2}(T \to 0)$ for the two orientations were used to find the zero-temperature coherence lengths, as shown in the figure.

where $a_1 = (\lambda_0 + \lambda_-)/2w$, $a_2 = (\lambda_0 - \lambda_-)/2w$, $\lambda_\pm = \lambda_{11} \pm \lambda_{22}$, $w = \lambda_{11}\lambda_{22} - \lambda_{12}\lambda_{21}$, and $\lambda_0 = (\lambda_-^2 + 4\lambda_{12}\lambda 21)^{1/2}$. Here λ_{ij} represents a coupling constant between bands i and j, and as the cross terms λ_{12} and λ_{21} only appear together, we set $\lambda_{21} = \lambda_{12}$ for simplicity. The values of the coupling constants allows us to establish the dominant pairing. For s^{++} pairing, for strong intraband coupling $w > 0$ [$w \sim 0.248$ for the case presented in Figs. 3(c) and 9(c)], whereas for strong interband coupling $w < 0$ [Figs. 3(a), 3(b), 9(a), and 9(b)]. Intraband pairing could indicate a nonsign changing order parameter (s^{++}) between different Fermi surfaces. However, many iron-based materials are dominated by strong interband pairing, suggestive of a sign changing order parameter ($s^{\pm}$).

U_1 and U_2 are defined as

$$U_1 = 2e^{q^2}\mathrm{Re}\sum_{n=0}^{\infty}\int_q^\infty \mathrm{d}u e^{-u^2} \times \left(\frac{u}{n+1/2} - \frac{t}{\sqrt{b}}\tan^{-1}\left[\frac{u\sqrt{b}}{t(n+1/2)+i\alpha b}\right]\right), \tag{A7}$$

$$U_2 = 2e^{q^2 s}\mathrm{Re}\sum_{n=0}^{\infty}\int_{q\sqrt{s}}^\infty \mathrm{d}u e^{-u^2} \times \left(\frac{u}{n+1/2} - \frac{t}{\sqrt{b\eta}}\tan^{-1}\left[\frac{u\sqrt{b\eta}}{t(n+1/2)+i\alpha b}\right]\right) \tag{A8}$$

The variables used for this two-band model, b, α, q, η, and s, are defined as

$$b = \frac{\hbar^2 v_1^2 H_{c2}}{8\pi\phi_0 {k_B}^2 T_c^2}, \quad \alpha = \frac{4\mu\phi_0 k_B T_c}{\hbar^2 v_1^2}, \quad q^2 = \frac{Q^2\phi_0\epsilon_1}{2\pi H_{c2}}, \quad \eta = \frac{v_2^2}{v_1^2}, \quad s = \frac{\epsilon_2}{\epsilon_1}. \tag{A9}$$

v_i is the in-plane Fermi velocity of band i, ϵ_i is the mass anisotropy ratio, $\epsilon_i = m_i^\perp/m_i^\parallel$ is related to the ratio between the gradients near T_c in different field orientations, s is band mass anisotropy between the two bands, and $\gamma = \epsilon^{-1/2}$. Various simulations of upper critical fields using this two-band model are shown in Fig. 8. The slope of H_{c2} near T_c of $CaKFe_4As_4$, is -3.3 for $H||c$ and -10.8 for $H||(ab)$, giving an $\epsilon \sim 1/10$. Q is the magnitude of the FFLO modulation and it is found for a given temperature when H_{c2} is maximal ($dH_{c2}/dQ = 0$). The simulations of H_{c2} for $H||(ab)$ assumed that the bands have the same anisotropy parameter $\epsilon_1 = \epsilon_2 = \epsilon$. Other parameters are estimated based on the fitted values using a single-band model and the velocities are minimized locally to find an optimum solution. This approach was used to infer the presence of either *interband* or *intraband* dominated pairings, as described in the main body.

A rescaling of the upper critical field has been performed previously mapping $H_{c2}^c \to H_{c2}^{ab}$ using $q_{ab} \to q_c\epsilon^{-3/4}$, $\alpha_{ab} \to \alpha_c\epsilon^{-1/2}$, $b_{ab}^{1/2} \to b_c^{1/2}\epsilon^{1/4}$ in U_1, $(\eta_{ab}b_{ab})^{1/2} \to (\eta_c b_c^{1/2})\epsilon^{1/4}$ in U_2. The values of the α parameters change as $\alpha_{ab,1} \to \alpha_c\epsilon^{-1/2}$ and $\alpha_{ab,2} \to \alpha/(\eta\epsilon^{1/2})$. However, this rescaling has not been used in this study, as the ratio between the Fermi velocities η is a variable parameter that can be changed between the two field orientations.

Previous studies on $CaKFe_4As_4$ have described the onset upper critical field data up to 60 T using the parameters $\lambda_{11} =$

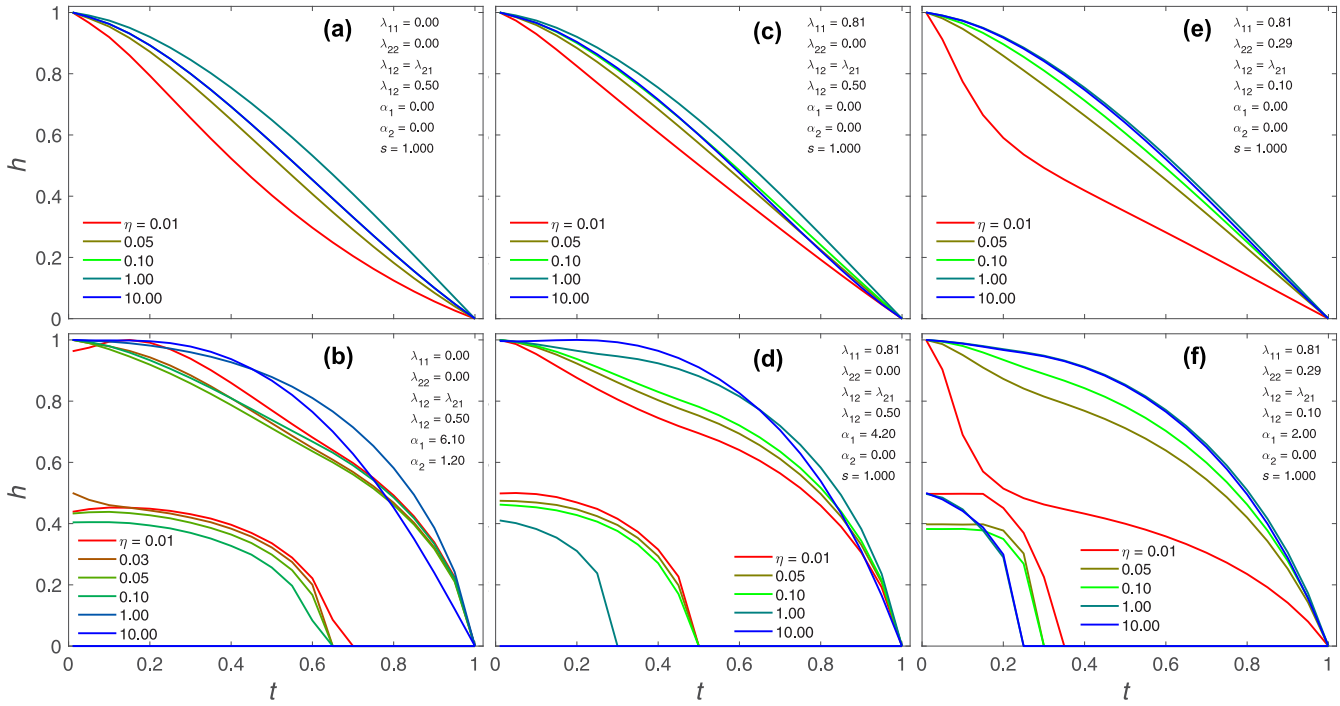

FIG. 8. Two-band upper-critical-field simulations for different band-coupling parameters and values of η. Simulations of the reduced upper critical field h using the two-band model based on Eqs. (A6)–(A9). The parameters listed in each panel correspond to $s^{\pm}$ pairing in (a) and (b) with $\lambda_{11} = \lambda_{22} = 0$, $\lambda_{12} = \lambda_{21} = 0.5$, $s^{\pm}$ pairing in (c) and (d) with $\lambda_{11} = \lambda_{22} = 0.81$, $\lambda_{12} = \lambda_{21} = 0.5$, and s^{++} pairing in (e) and (f) with $\lambda_{11} = 0.81$, $\lambda_{22} = 0.29$, and $\lambda_{12} = \lambda_{21} = 0.1$, $\alpha_1 = 0.95$ for $H||c$. For panels (b), (d), and (f) the lower curves (left corners) represent the magnitude of the FFLO modulation, $Q/(2Q(0))$.

$\lambda_{22} = 0$, $\lambda_{12}\lambda_{21} = 0.25$, $\eta = 0.2$, $\alpha = 0.5$, $\epsilon = 1/6$, and the above rescaling [7]. Using these parameters, we find that the onset upper critical field data (open blue and red symbols) clearly fail to describe the full temperature dependence of the upper critical field of $CaKFe_4As_4$, as shown in Figs. 9(a) and 9(b) (blue and red curves). As discussed in the main body of text, we can reasonably describe the upper critical field of $CaKFe_4As_4$ using a two-band model with band parameters for the $s^{\pm}$ and s^{++} pairing (see Table I), as shown in Figs. 9(c) and 9(e), respectively. We note here that an FFLO state can be stabilized at low temperatures for $H||(ab)$ [Figs. 9(c) and 9(e), right axis].

To further test the obtained parameters, we have modelled both the offset and onset critical fields for both field orientations assuming the $s^{\pm}$ and s^{++} pairing. The parameters for the two cases are listed in Table I and the simulations of the upper critical field are shown in Fig. 9. We find that the parameters describing the offset and onset upper critical fields are similar, with small differences found for the α values, which are slightly larger as the curvature for H_{on} is greater as compared with the H_{off} case. The velocities for H_{on} are also slightly smaller due to the larger slopes near T_c, which scales as $|dH_{c2}/dT|_{T_c} \propto 1/v^2$. Using the values for H_{off} and H_{on}, we expected a ∼20% difference in velocities when $H||c$

TABLE I. The different parameters used for the simulations of the upper critical field (defined either using an offset or onset magnetic field), using a two-band model and considering different pairing symmetries and magnetic field orientations in $CaKFe_4As_4$.

	$\mu_0 H_{off}$				$\mu_0 H_{on}$			
	$s^{\pm}$		s^{++}		$s^{\pm}$		s^{++}	
	$H||c$	$H||(ab)$	$H||c$	$H||(ab)$	$H||c$	$H||(ab)$	$H||c$	$H||(ab)$
λ_{11}	0	0	0.81	0.81	0	0	0.81	0.81
λ_{22}	0	0	0.29	0.29	0	0	0.29	0.29
λ_{12}	0.5	0.5	0.1	0.1	0.5	0.5	0.1	0.1
α_1	0.95	3.1	0.5	3.2	1.5	4.2	1.0	3.5
α_2	0	0.7	0	0	0	0	0	0
v_1 (meVÅ)	510(20)	253(20)	380(20)	195(20)	400(20)	215(20)	312(20)	181(20)
v_2 (meVÅ)	40(4)	51(5)	54(4)	41(4)	36(3)	43(4)	44(4)	38(4)
η	∼0.006	∼0.04	∼0.02	∼0.04	∼0.008	∼0.04	∼0.02	∼0.045

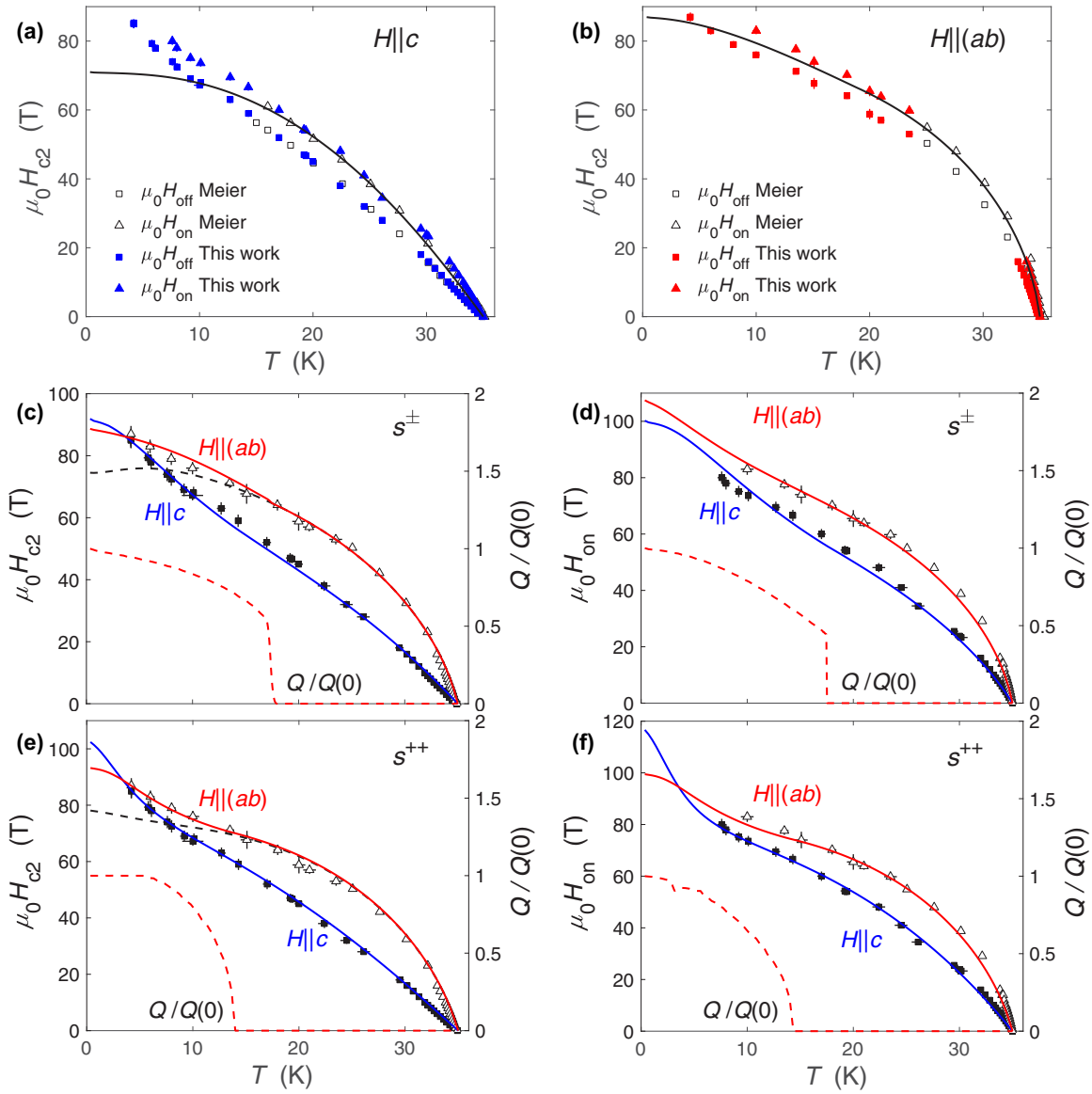

FIG. 9. Two-band upper-critical-field models for $CaKFe_4As_4$ using different band-coupling parameters. (a), (b) $\lambda_{11} = \lambda_{22} = 0$, $\lambda_{12}\lambda_{21} = 0.25$, $\eta = 0.2$, $\alpha = 0.5$, and $\epsilon = 1/6$ used previously to describe the onset upper critical field of $CaKFe_4As_4$ up to 60 T [7] when $H||c$ and $H||(ab)$, respectively. (c) $s^{\pm}$ pairing with $\lambda_{11} = \lambda_{22} = 0$, $\lambda_{12} = \lambda_{21} = 0.5$. Here $\alpha_1 = 0.95$, $\alpha_2 = 0$, and $\eta \sim 0.006$ for $H||c$, and $\alpha_1 = 3.1$, $\alpha_2 = 0.7$, and $\eta \sim 0.04$ for $H||(ab)$. (d) $s^{\pm}$ pairing for the onset critical field using the same parameters as in (c), but with $\eta \sim 0.008$ and $\alpha_1 = 1.5$ when $H||c$ and $\alpha_1 = 4.2$ when $H||(ab)$. (e) s^{++} pairing with $\lambda_{11} = 0.81$, $\lambda_{22} = 0.29$, and $\lambda_{12} = \lambda_{21} = 0.1$. Here $\alpha_1 = 0.95$, $\alpha_2 = 0$, and $\eta \sim 0.02$ for $H||c$, and $\alpha_1 = 3.1$, $\alpha_2 = 0.0$ and $\eta \sim 0.04$ for $H||(ab)$. (f) s^{++} pairing for the onset critical field using the same parameters as in (e), but with $\alpha_1 = 1.0$ when $H||c$, and $\alpha_1 = 3.5$ when $H||(ab)$. In (c)–(f), blue lines show the two-band model (with no FFLO state present) when $H||c$, dashed black lines show the two-band model with no FFLO state when $H||(ab)$, and the red lines show the two-band model with an FFLO state when $H||(ab)$. The temperature dependence of the FFLO Q vector is shown by the dashed red lines (the right axis in (c)–(f)) for $H||(ab)$, and it is scaled to the zero-temperature value $Q(0)$. We note that the FFLO state emerges when $H||(ab)$, regardless of the pairing limit or which critical field criteria is chosen. This reinforces the robustness of this result.

and a ∼10% difference when $H||(ab)$, as shown in Table I. However, independent of the definition of the upper critical field, the stabilization of an FFLO state in $CaKFe_4As_4$ for $H||(ab)$ is realized in both cases.

[1] A. Gurevich, Upper critical field and the Fulde-Ferrell-Larkin-Ovchinnikov transition in multiband superconductors, Phys. Rev. B **82**, 184504 (2010).

[2] K. W. Song and A. E. Koshelev, Quantum FFLO State Iclean Layered Superconductors, Phys. Rev. X **9**, 021025 (2019).

[3] P. J. Hirschfeld, M. M. Korshunov, and I. I. Mazin, Gap symmetry and structure of Fe-based superconductors, Rep. Prog. Phys. **74**, 124508 (2011).

[4] D. Mou, T. Kong, W. R. Meier, F. Lochner, L.-L. Wang, Q. Lin, Y. Wu, S. L. Bud'ko, I. Eremin, D. D. Johnson, P. C. Canfield, and A. Kaminski, Enhancement of the Superconducting Gap by Nesting in $CaKFe_4As_4$: A New High Temperature Superconductor, Phys. Rev. Lett. **117**, 277001 (2016).

[5] A. Iyo, K. Kawashima, T. Kinjo, T. Nishio, S. Ishida, H. Fujihisa, Y. Gotoh, K. Kihou, H. Eisaki, and Y. Yoshida, New-structure-type Fe-based superconductors: Ca$A$$Fe_4As_4$ (A = K, Rb, Cs) and Sr$A$$Fe_4As_4$ (A = Rb, Cs), J. Am. Chem. Soc. **138**, 3410 (2016).

[6] K. Iida, M. Ishikado, Y. Nagai, H. Yoshida, A. D. Christianson, N. Murai, K. Kawashima, Y. Yoshida, H. Eisaki, and A. Iyo, Spin resonance in the new-structure-type iron-based superconductor $CaKFe_4As_4$, J. Phys. Soc. Jpn. **86**, 093703 (2017).

[7] W. R. Meier, T. Kong, U. S. Kaluarachchi, V. Taufour, N. H. Jo, G. Drachuck, A. E. Böhmer, S. M. Saunders, A. Sapkota, A. Kreyssig, M. A. Tanatar, R. Prozorov, A. I. Goldman, F. F. Balakirev, A. Gurevich, S. L. Bud'ko, and P. C. Canfield, Anisotropic thermodynamic and transport properties of single crystalline $CaKFe_4As_4$, Phys. Rev. B **94**, 064501 (2016).

[8] S. L. Bud'ko, T. Kong, W. R. Meier, X. Ma, and P. C. Canfield, 57Fe Mössbauer study of stoichiometric iron-based superconductor $CaKFe_4As_4$: A comparison to KFe_2As_2 and $CaFe_2As_2$, Philos. Mag. **97**, 2689 (2017).

[9] S. L. Bud'ko, V. G. Kogan, R. Prozorov, W. R. Meier, M. Xu, and P. C. Canfield, Coexistence of superconductivity and magnetism in $CaK(Fe_{1-x}Ni_x)_4As_4$ as probed by ^{57}Fe Mössbauer spectroscopy, Phys. Rev. B **98**, 144520 (2018).

[10] J. Cui, Q.-P. Ding, W. R. Meier, A. E. Böhmer, T. Kong, V. Borisov, Y. Lee, S. L. Bud'ko, R. Valentí, P. C. Canfield, and Y. Furukawa, Magnetic fluctuations and superconducting properties of $CaKFe_4As_4$ studied by ^{75}As NMR, Phys. Rev. B **96**, 104512 (2017).

[11] W.-L. Zhang, W. R. Meier, T. Kong, P. C. Canfield, and G. Blumberg, High-T_c superconductivity in $CaKFe_4As_4$ in absence of nematic fluctuations, Phys. Rev. B **98**, 140501(R) (2018).

[12] Q.-P. Ding, W. R. Meier, A. E. Böhmer, S. L. Bud'ko, P. C. Canfield, and Y. Furukawa, NMR study of the new magnetic superconductor $CaK(Fe_{0.951}Ni_{0.049})_4As_4$: Microscopic coexistence of the hedgehog spin-vortex crystal and superconductivity, Phys. Rev. B **96**, 220510(R) (2017).

[13] Q.-P. Ding, W. R. Meier, J. Cui, M. Xu, A. E. Böhmer, S. L. Bud'ko, P. C. Canfield, and Y. Furukawa, Hedgehog Spin-Vortex Crystal Antiferromagnetic Quantum Criticality in $CaK(Fe_{1-x}Ni_x)_4As_4$ Revealed by NMR, Phys. Rev. Lett. **121**, 137204 (2018).

[14] S. J. Singh, M. Bristow, W. R. Meier, P. Taylor, S. J. Blundell, P. C. Canfield, and A. I. Coldea, Ultrahigh critical current densities, the vortex phase diagram, and the effect of granularity of the stoichiometric high-T_c superconductor $CaKFe_4As_4$, Phys. Rev. Mater. **2**, 074802 (2018).

[15] N. Haberkorn, M. Xu, W. R. Meier, J. Schmidt, S. L. Bud'ko, and P. C. Canfield, Effect of Ni doping on vortex pinning in $CaK(Fe_{1-x}Ni_x)_4As_4$ single crystals, Phys. Rev. B **100**, 064524 (2019).

[16] S. Ishida, A. Iyo, H. Ogino, H. Eisaki, N. Takeshita, K. Kawashima, K. Yanagisawa, Y. Kobayashi, K. Kimoto, H. Abe, M. Imai, Jun-ichi Shimoyama, and M. Eisterer, Unique defect structure and advantageous vortex pinning properties in superconducting CaKFe4As4, npj Quantum Mater. **4**, 27 (2019).

[17] W. R. Meier, T. Kong, S. L. Bud'ko, and P. C. Canfield, Optimization of the crystal growth of the superconductor $CaKFe_4As_4$ from solution in the $FeAs-CaFe_2As_2-KFe_2As_2$ system, Phys. Rev. Mater. **1**, 013401 (2017).

[18] A. Serafin, A. I. Coldea, A. Y. Ganin, M. J. Rosseinsky, K. Prassides, D. Vignolles, and A. Carrington, Anisotropic fluctuations and quasiparticle excitations in $FeSe_{0.5}Te_{0.5}$, Phys. Rev. B **82**, 104514 (2010).

[19] D. Braithwaite, G. Lapertot, W. Knafo, and I. Sheikin, Evidence for anisotropic vortex dynamics and Pauli limitation in the upper critical field of $FeSe_{1-x}Te_x$, J. Phys. Soc. Jpn. **79**, 053703 (2010).

[20] H. Q. Yuan, J. Singleton, F. F. Balakirev, S. A. Baily, G. F. Chen, J. L. Luo, and N. L. Wang, Nearly isotropic superconductivity in $(Ba,K)Fe_2As_2$, Nature **457**, 565 (2009).

[21] K. Hashimoto, A. Serafin, S. Tonegawa, R. Katsumata, R. Okazaki, T. Saito, H. Fukazawa, Y. Kohori, K. Kihou, C. H. Lee, A. Iyo, H. Eisaki, H. Ikeda, Y. Matsuda, A. Carrington, and T. Shibauchi, Evidence for superconducting gap nodes in the zone-centered hole bands of KFe_2As_2 from magnetic penetration-depth measurements, Phys. Rev. B **82**, 014526 (2010).

[22] D. V. Suetin and I. R. Shein, Electronic properties and Fermi surface for new layered high-temperature superconductors CaAFe4As4 (A = K, Rb, and Cs): FLAPW-GGA calculations, J. Supercond. Novel Magn. **31**, 1683 (2018).

[23] A. Fente, W. R. Meier, T. Kong, V. G. Kogan, S. L. Bud'ko, P. C. Canfield, I. Guillamón, and H. Suderow, Influence of multiband sign-changing superconductivity on vortex cores and vortex pinning in stoichiometric high-$T_c$$CaKFe_4As_4$, Phys. Rev. B **97**, 134501 (2018).

[24] M. Tinkham, *Introduction to Superconductivity*, 2nd ed. (Dover Publications, Mineola, New York, 2004).

[25] N. R. Werthamer, E. Helfand, and P. C. Hohenberg, Temperature and purity dependence of the superconducting critical field, H_{c2}. III. electron spin and spin-orbit effects, Phys. Rev. **147**, 295 (1966).

[26] E. Helfand and N. R. Werthamer, Temperature and purity dependence of the superconducting critical field, H_{c2}. II, Phys. Rev. **147**, 288 (1966).

[27] S. Khim, J. W. Kim, E. S. Choi, Y. Bang, M. Nohara, H. Takagi, and K. H. Kim, Evidence for dominant Pauli paramagnetic effect in the upper critical field of single-crystalline $FeTe_{0.6}Se_{0.4}$, Phys. Rev. B **81**, 184511 (2010).

[28] C. Tarantini, A. Gurevich, J. Jaroszynski, F. Balakirev, E. Bellingeri, I. Pallecchi, C. Ferdeghini, B. Shen, H. H. Wen, and D. C. Larbalestier, Significant enhancement of upper critical fields by doping and strain in iron-based superconductors, Phys. Rev. B **84**, 184522 (2011).

[29] K. Cho, H. Kim, M. A. Tanatar, Y. J. Song, Y. S. Kwon, W. A. Coniglio, C. C. Agosta, A. Gurevich, and R.

Prozorov, Anisotropic upper critical field and possible Fulde-Ferrell-Larkin-Ovchinnikov state in the stoichiometric pnictide superconductor LiFeAs, Phys. Rev. B **83**, 060502(R) (2011).

[30] A. Gurevich, Iron-based superconductors at high magnetic fields, Rep. Prog. Phys. **74**, 124501 (2011).

[31] B. Maiorov, P. Mele, S. A. Baily, M. Weigand, S. Z. Lin, F. F. Balakirev, K. Matsumoto, H. Nagayoshi, S. Fujita, Y. Yoshida, Y. Ichino, T. Kiss, A. Ichinose, M. Mukaida, and L. Civale, Inversion of the upper critical field anisotropy in FeTeS films, Supercond. Sci. Technol. **27**, 044005 (2014).

[32] G. Fuchs, S. L. Drechsler, N. Kozlova, M. Bartkowiak, J. E. Hamann-Borrero, G. Behr, K. Nenkov, H. H. Klauss, H. Maeter, A. Amato, H. Luetkens, A. Kwadrin, R. Khasanov, J. Freudenberger, A. Köhler, M. Knupfer, E. Arushanov, H. Rosner, B. Büchner, and L. Schultz, Orbital and spin effects for the upper critical field in As-deficient disordered Fe pnictide superconductors, New J. Phys. **11**, 075007 (2009).

[33] R. Khasanov, W. R. Meier, Y. Wu, D. Mou, S. L. Bud'ko, I. Eremin, H. Luetkens, A. Kaminski, P. C. Canfield, and A. Amato, In-plane magnetic penetration depth of superconducting $CaKFe_4As_4$, Phys. Rev. B **97**, 140503(R) (2018).

[34] M. Kano, Y. Kohama, D. Graf, F. Balakirev, A. S. Sefat, M. A. Mcguire, B. C. Sales, D. Mandrus, and S. W. Tozer, Anisotropy of the upper critical field in a Co-doped $BaFe_2As_2$ single crystal, J. Phys. Soc. Jpn. **78**, 084719 (2009).

[35] M. Bristow, Upper critical fields across the nematic end point in $FeSe_{1-x}S_x$ (private communication, 2020).

[36] H. Kontani and S. Onari, Orbital-Fluctuation-Mediated Superconductivity in Iron Pnictides: Analysis of the Five-Orbital Hubbard-Holstein Model, Phys. Rev. Lett. **104**, 157001 (2010).

[37] D. V. Efremov, M. M. Korshunov, O. V. Dolgov, A. A. Golubov, and P. J. Hirschfeld, Disorder-induced transition between $s_{\pm}$ and s_{++} states in two-band superconductors, Phys. Rev. B **84**, 180512(R) (2011).

[38] A. A. Golubov, J. Kortus, O. V. Dolgov, O. Jepsen, Y. Kong, O. K. Andersen, B. J. Gibson, K. Ahn, and R. K. Kremer, Specific heat of MgB_2 in a one- and a two-band model from first-principles calculations, J. Phys.: Condens. Matter **14**, 1353 (2002).

[39] L. W. Gruenberg and L. Gunther, Fulde-Ferrell Effect in Type-II Superconductors, Phys. Rev. Lett. **16**, 996 (1966).

[40] T. Saito, Y. Yamakawa, S. Onari, and H. Kontani, Revisiting orbital-fluctuation-mediated superconductivity in LiFeAs: Nontrivial spin-orbit interaction effects on the band structure and superconducting gap function, Phys. Rev. B **92**, 134522 (2015).

[41] F. Lochner, F. Ahn, T. Hickel, and I. Eremin, Electronic properties, low-energy Hamiltonian, and superconducting instabilities in $CaKFe_4As_4$, Phys. Rev. B **96**, 094521 (2017).

[42] https://doi.org/10.5287/bodleian:dmRar8AgJ.

[43] http://www.cfas.ox.ac.uk/.